

RESEARCH ARTICLE

10.1029/2020JD033862

Methyl Chloroform Continues to Constrain the Hydroxyl (OH) Variability in the Troposphere

Key Points:

- High-quality measurements of CH_3CCl_3 from two independent measurement networks provide key information about tropospheric OH variability
- We separate effects of the “physical” climate on inverse lifetime of CH_3CCl_3 (K_G) from those arising from “chemical” changes in the atmosphere
- Robust variability in K_G , correlating with the El Niño Southern Oscillation, has large implications, e.g., for the global methane budget

Supporting Information:

Supporting Information may be found in the online version of this article.

Correspondence to:

P. K. Patra and M. C. Krol,
prabir@jamstec.go.jp;
Maarten.Krol@wur.nl

Citation:












Patra, P. K., Krol, M. C., Prinn, R. G., Takigawa, M., Mühle, J., Montzka, S. A., et al. (2021). Methyl chloroform continues to constrain the hydroxyl (OH) variability in the troposphere. *Journal of Geophysical Research: Atmospheres*, 126, e2020JD033862. <https://doi.org/10.1029/2020JD033862>

Received 10 SEP 2020

Accepted 23 DEC 2020

Author Contributions:

Conceptualization: M. C. Krol, R. G. Prinn, M. Takigawa, S. A. Montzka, Y. Yamashita, J. W. Elkins
Data curation: J. Mühle, S. A. Montzka, S. Lal, R. F. Weiss, P. B. Krummel, P. J. Fraser, S. O'Doherty, J. W. Elkins
Formal analysis: M. C. Krol, N. Chandra, P. B. Krummel
Investigation: M. C. Krol, R. G. Prinn, P. J. Fraser
Methodology: R. G. Prinn, M. Takigawa, J. Mühle, Y. Yamashita, S. Naus
Resources: R. F. Weiss, P. J. Fraser, J. W. Elkins
Software: M. Takigawa, N. Chandra
Validation: S. Naus
Visualization: N. Chandra

P. K. Patra^{1,2} , M. C. Krol^{3,4} , R. G. Prinn⁵ , M. Takigawa¹ , J. Mühle⁶ , S. A. Montzka⁷ , S. Lal⁸, Y. Yamashita^{1,9} , S. Naus³ , N. Chandra^{1,9}, R. F. Weiss⁶ , P. B. Krummel¹⁰ , P. J. Fraser¹⁰, S. O'Doherty¹¹ , and J. W. Elkins⁷

¹Research Institute for Global Change, Japan Agency for Marine–Earth Sciences and Tech. (JAMSTEC), Yokohama, Japan, ²Center for Environmental Remote Sensing, Chiba University, Chiba, Japan, ³Meteorology and Air Quality Group, Wageningen University, Wageningen, The Netherlands, ⁴Institute for Marine and Atmospheric Research Utrecht, Utrecht University, Utrecht, The Netherlands, ⁵Massachusetts Institute of Technology, Cambridge, MA, USA, ⁶Scripps Institution of Oceanography, University of California, San Diego, CA, USA, ⁷NOAA Global Monitoring Laboratory, Boulder, CO, USA, ⁸Physical Research Laboratory, Ahmedabad, Gujarat, India, ⁹Now at National Institute for Environmental Studies, Tsukuba, Japan, ¹⁰Climate Science Centre, CSIRO Oceans and Atmosphere, Aspendale, VIC, Australia, ¹¹School of Chemistry, University of Bristol, Bristol, UK

Abstract Trends and variability in tropospheric hydroxyl (OH) radicals influence budgets of many greenhouse gases, air pollutant species, and ozone depleting substances. Estimations of tropospheric OH trends and variability based on budget analysis of methyl chloroform (CH_3CCl_3) and process-based chemistry transport models often produce conflicting results. Here we use a previously tested transport model to simulate atmospheric CH_3CCl_3 for the period 1985–2018. Based on mismatches between model output and observations, we derive consistent anomalies in the inverse lifetime of CH_3CCl_3 (K_G) using measurements from two independent observational networks (National Oceanic and Atmospheric Administration and Advanced Global Atmospheric Gases Experiment). Our method allows a separation between “physical” (transport, temperature) and “chemical” (i.e., abundance) influences on $\text{OH} + \text{CH}_3\text{CCl}_3$ reaction rate in the atmosphere. Small increases in K_G due to “physical” influences are mostly driven by increases in the temperature-dependent reaction between OH and CH_3CCl_3 and resulted in a smoothly varying increase of 0.80% decade⁻¹. Chemical effects on K_G , linked to global changes in OH sources and sinks, show larger year-to-year variations (~2%–3%), and have a negative correlation with the El Niño Southern Oscillation. A significant positive trend in K_G can be derived after 2001, but it persists only through 2015 and only if we assume that CH_3CCl_3 emissions decayed more slowly over time than our best estimate suggests. If global CH_3CCl_3 emissions dropped below 3 Gg year⁻¹ after 2015, recent CH_3CCl_3 measurements indicate that the 2015–2018 loss rate of CH_3CCl_3 due to reaction with OH is comparable to its value 2 decades ago.

1. Introduction

Hydroxyl radicals are primarily produced in the Earth's atmosphere through the reaction of water vapor (H_2O) with an excited state oxygen atom (O^1D). O^1D is produced through the photodissociation of atmospheric ozone (O_3) by solar ultraviolet radiation (Seinfeld & Pandis, 2006). Equally important is secondary OH production (recycling) in determining the availability of OH in the troposphere, involving many chemical reactions of organic and inorganic species (Lelieveld et al., 2002). The OH free radical is central to tropospheric air pollution chemistry and is responsible for removal of multiple greenhouse gases, ozone depleting substances, and air pollutants (Crutzen & Zimmermann, 1991; Levy, 1971; Prather & Spivakovsky, 1990; Singh et al., 1995). A precise knowledge of the global mean abundance, trend, and interannual variability of OH is needed to estimate source and sink budgets of greenhouse gases and ozone depleting substances, such as methane (CH_4), hydrogen containing halocarbons (e.g., methyl halides, hydrofluorocarbons (HFCs), hydrochlorofluorocarbons (HCFCs)), and methyl chloroform (CH_3CCl_3) (Krol & Lelieveld, 2003; Lovelock, 1977; Makide & Rowland, 1981; Montzka et al., 2011; Naik et al., 2013; Patra et al., 2011; Prinn et al., 1992, 2001, 2005). The current lack of understanding of the causes for the observed CH_4 growth rate variability over recent decades has created further incentives for better estimation of OH trends and variability (Rigby et al., 2017; Turner et al., 2017; Zhao et al., 2019).

Due to the strong reactivity of OH in the atmosphere within a given air parcel, it has a short lifetime, typically ~1 s, and observation-based (re)construction of spatial distribution and temporal trends have remained

Writing – original draft: M. C. Krol, R. G. Prinn, J. Mühle, S. A. Montzka
Writing – review & editing: S. Lal, P. B. Krummel, P. J. Fraser

elusive. As a result, space-time variations of OH are estimated indirectly using tracers such as CH_3CCl_3 (Krol & Lelieveld, 2003; Montzka, 2000; Montzka et al., 2011; Patra et al., 2014; Prinn et al., 1992, 2001, 2005), ^{14}CO (Brenninkmeijer et al., 1992; Krol et al., 2008), and, more recently, satellite-derived HCHO and isoprene (Wells et al., 2020; Wolfe et al., 2019). Alternatively, simulations with global chemistry transport models (CTMs) are used to estimate the mean abundance, trend, and variability in OH (Dalsøren et al., 2016; Murray et al., 2014; Naik et al., 2013; Stevenson et al., 2020; Voulgarakis et al., 2013; Zhao et al., 2019). However, due to the uncertainties in precursor emissions, for example, of volatile organic compounds and nitrogen oxides (NO_x), and in modeled processes, it is difficult to accurately simulate OH (Gaubert et al., 2017; Lelieveld et al., 2018; Nguyen et al., 2020; Wolfe et al., 2019), and models often produce OH variabilities which are inconsistent with indirect estimations (He et al., 2020; Stevenson et al., 2020).

Due to the ambiguity of recent model studies that derived global OH variability and trends from CH_3CCl_3 (Naus et al., 2019; Rigby et al., 2017; Turner et al., 2017), a recent study (Nicely et al., 2020) states that “current observations are insufficient to unambiguously derive current trends in OH.” This corroborates earlier findings suggesting inconsistent phasing in CH_3CCl_3 -derived OH variability from year-to-year using data from different measurement networks and also when compared to full CTMs (Holmes et al., 2013; McNorton et al., 2016). Despite these issues, however, these CTM studies also concluded that CH_3CCl_3 -derived OH variations from the Advanced Global Atmospheric Gases Experiment (AGAGE) and National Oceanic and Atmospheric Administration (NOAA) networks provided useful insights into long-term atmospheric CH_4 variations (Montzka et al., 2011; Rigby et al., 2017; Turner et al., 2017).

Most studies that used measured CH_3CCl_3 to derive global mean OH trends and variability were performed with simplified multibox models (Rigby et al., 2017; Turner et al., 2017). As discussed in detail in Naus et al. (2019), this might lead to systematic biases in OH trends and variability, as box model approaches of chemical tracer simulations do not account for the heterogeneity and variability in emissions, chemistry, and transport. Moreover, by using box-averaged observations, it is likely that information from the collected CH_3CCl_3 time series has not been utilized to its full potential for deriving information about OH. It is most appropriate to use three-dimensional CTMs to infer the time evolution of two-dimensional OH variations (Bousquet et al., 2005; Naus et al., 2020). In this study, we take an intermediate approach where a three-dimensional model is used for the forward simulations, and global mean OH trends and variabilities are estimated from site-specific model-observation differences.

We use simulations of CH_3CCl_3 by the JAMSTEC's Model for Interdisciplinary Research On Climate (MIROC, version 4.0) atmospheric chemistry-transport model (MIROC4-ACTM) (Patra et al., 2018). First, we infer interannual variability (IAV) and trends in OH from the observation-model differences of CH_3CCl_3 mole fractions for sites located far away from source regions (next Section, Materials and Methods), then we discuss the implications of our findings for understanding the OH variability of the whole troposphere (Section 3, Results and discussion), followed up by major conclusions (Section 4).

2. Materials and Methods

2.1. MIROC4-ACTM

The MIROC4-ACTM is run at T42 horizontal resolution (approximately 2.8 degrees in latitude and longitude grid spacing). The model adapted a hybrid σ -pressure vertical coordinate system that consists of 67 layers, which enables a fully resolved description of the stratosphere and mesosphere (Watanabe et al., 2008). To drive tracer transport in the ACTM, meteorological fields of turbulent diffusion, temperature, convection, and advection are generated by the MIROC4 general circulation model forced by monthly mean sea-surface temperature variations. To better represent synoptic transport, horizontal winds and temperature of the ACTM at the altitude range of ~ 980 – 0.018 hPa are nudged with Japan Meteorological Agency Reanalysis (JRA-55) data products (Kobayashi et al., 2015). The performance of interhemispheric exchange rate and stratospheric mixing time in MIROC4-ACTM has been tested using nonreactive gases, for example, sulfur hexafluoride (SF_6) in the troposphere and carbon dioxide (CO_2) in the stratosphere (Patra et al., 2018). The model-observation comparisons of intersite differences in SF_6 (Supporting Information [S1], Figure S1) provide evidence that MIROC4-ACTM, nudged to the JRA-55, correctly represents features of interhemispheric and regional transport processes related to climate variations, including those related to El Niño Southern Oscillation (ENSO) (Francey et al., 2019; Patra

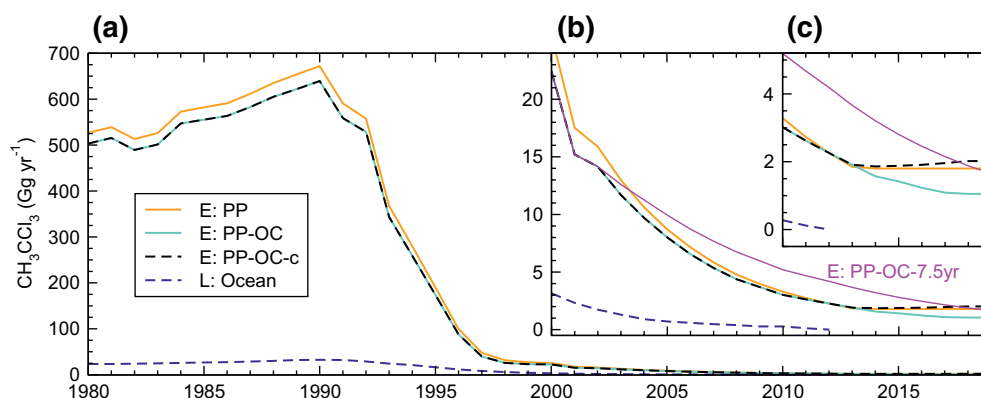


Figure 1. Time evolution of methyl chloroform (CH_3CCl_3) net emission (E) scenarios used in MIROC4-ACTM simulations (a; see Table S1 for annual mean values). The atmosphere-ocean flux (L—loss to ocean) is also shown. The insets (b and c) show emissions from 2000 (b) and 2010 (c) onwards, respectively, with zoomed-in y-axis.

et al., 2011). An accurate ENSO cycle is important in modeling CH_3CCl_3 observations (Prinn et al., 1992). Note that the JRA-55 meteorological fields are also used to calculate the multivariate ENSO index, version 2 (MEI.v2; www.esrl.noaa.gov/psd/enso/mei/) (Wolter & Timlin, 2011).

To simulate mole fractions of CH_3CCl_3 at measurement locations during 1985–2018, the model uses offline OH fields and several emission scenarios as described below. All the model simulations are initiated at January 1, 1981, using an initial model field generated by a 20-year spin-up simulation (1981–2000). This spin-up period is used to set up proper concentration profiles in the stratosphere. The period 1981–1984 is considered as a secondary spin-up period to equilibrate CH_3CCl_3 sources and sinks with transport. Model simulations from 1985–2018 are used for our analysis.

2.2. CH_3CCl_3 Emissions and Oceanic Sinks

The time evolution of annual-mean emissions is based on industrial emission inventory information for 1980–2000 (McCulloch & Midgley, 2001) and subsequent extrapolations to 2001–2019 as discussed below. No seasonality in the emissions is considered here. In contrast to previous 3D model simulations in which ocean loss was parametrized as a first order deposition process (Patra et al., 2011, 2014), we have now used the global total oceanic flux of CH_3CCl_3 for the period of 1980–2000 from Wennberg et al. (2004), albeit with the CO_2 flux patterns in two sensitivity studies (PP-OC, PP-OC-c). These simulations account for the fact that CH_3CCl_3 that dissolved in the ocean during the 1980s and early 1990s may start to reenter the atmosphere on the net in the late 1990s, because the atmospheric CH_3CCl_3 abundance has dropped since 1998 at a faster rate than dissolved CH_3CCl_3 . To account for the larger CH_3CCl_3 solubility in cold ocean water (Butler et al., 1991), we have spatially distributed the global total yearly sinks from that study using the CO_2 flux pattern (Takahashi et al., 2009). The spatial distribution using proxy CO_2 flux pattern is performed because the CH_3CCl_3 flux map data were not archived digitally from Wennberg et al. (2004) (Paul Wennberg, personal communication, June 2019). After 2000, we assume a linearly decreasing oceanic loss with zero deposition from 2012 onwards. The following emission scenarios are prepared for the simulation period 1981–2018 (Figure 1):

Case PP: Anthropogenic emissions are taken from Patra et al. (2014) for 1980–2013. After following reported industrial emissions (McCulloch & Midgley, 2001), the emissions are extended for 2001–2013 with an exponential decay with a decay constant of 5 years. Emissions between 2014 and 2019 are kept constant.

Case PP-OC: As case PP, but with the ocean sink OC subtracted. Anthropogenic emissions between 2014 and 2019 continue to decrease in time. Oceanic sink is distributed using Takahashi et al. (2009) flux pattern.

Case PP-OC-c: As PP-OC, but anthropogenic emissions between 2014 and 2019 increase slightly. Oceanic sink is distributed uniformly over all ocean grids. This will be used as our control case for this analysis. A mild increase in emissions over the recent 5 years is also suggested by joint OH-emission inversion (Naus et al., 2020).

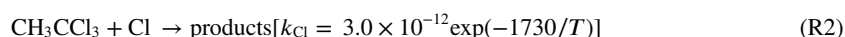
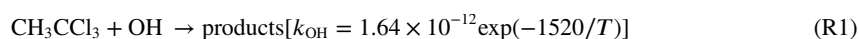
Case PP-OC-7.5 years: Same as PP-OC, but now the anthropogenic emissions are extended for 2001–2019 with an exponential decay with a decay constant of 7.5 years. This scenario is used to check the influence of the uncertainty in the emission drop after 2001 on the inferred OH trend.

The numerical values of anthropogenic emissions (with ocean uptake subtracted for Case PP-OC and PP-OC-c) are given in the SI Table S1. The effects of oceanic sink and its patterns on CH₃CCl₃ simulations are shown in Figure S2 and discussed in Section 3.3. Figure 1 shows the time evolution of the globally integrated surface flux applied in the four scenarios.

2.3. OH Fields and Chemical Reactions

We use predefined tropospheric OH concentrations at monthly mean time intervals (Spivakovsky et al., 2000), after scaling the global totals by 0.92 to simulate global CH₃CCl₃ decay rates as in the TransCom-CH₄ experiment (Control OH, which has the NH/SH OH ratio of 0.99 [Patra et al., 2011], with the Northern and Southern Hemispheres [NH, SH] delineated at the equator). These predefined OH concentrations (Spivakovsky et al., 2000) were derived with a semi-empirical method to estimate seasonally varying OH fields using observed distributions of O₃, H₂O, NO_{x,ir} (total reactive nitrogen oxides), CO, hydrocarbons, temperature, and cloud optical depth. The OH field for the altitudes above 100 hPa are taken from a CTM simulation of stratospheric ozone chemistry (Takigawa et al., 1999).

We have considered the following reactions to simulate OH chemistry and stratospheric photolysis (*J*)



with k_{OH} and k_{Cl} being the temperature dependent rate constant of CH₃CCl₃ with OH and Cl, respectively (Burkholder et al., 2015). A climatological Cl field for the stratosphere at monthly time interval is taken from Takigawa et al. (1999). The photolysis rate *J* is calculated online by parameterizing the ultraviolet (UV) absorption cross sections of CH₃CCl₃ from the database of Chemical Kinetics and Photochemical Data for Use in Atmospheric Studies (Burkholder et al., 2015).

2.4. CH₃CCl₃ Measurements and Data Processing

Measurements of CH₃CCl₃ are taken from five sites of the AGAGE (AGAGE; and its predecessors: the Atmospheric Lifetime Experiment, ALE, and the Global Atmospheric Gases Experiment, GAGE; Table 1) in situ monitoring network (Prinn et al., 2000, 2018). The gas chromatograph-multi detector (GC-MD) instruments use an electron capture detector (ECD) to make a calibrated air measurement of CH₃CCl₃ every 3 h (ALE), 2 h (GAGE), and 40 min (AGAGE), respectively. The “Medusa” instrument preconcentrates 2 L of air over 20 min with analysis by GC-MS (gas chromatography - mass spectrometry), leading to a calibrated ambient air measurement every 2 h (Arnold et al., 2012; Miller et al., 2008). All AGAGE measurements are reported on the SIO-05 gravimetric calibration scale. Additionally, we use discrete measurements from flasks collected by the NOAA halocarbon and other trace species (HATS) flask sampling network at 12 locations (Table 1) (Montzka et al., 2011). All HATS flask air samples are analyzed with a single GC-MS system at the NOAA laboratory in Boulder and the measurements for all sites are calibrated with respect to the same reference standard scale.

We use balloon-borne cryo-sampling observations from Hyderabad, India (Lal et al., 1994), and an observational data product from Gap, France (Fabian et al., 1996) for evaluation of the model simulated photo-chemical loss and transport of CH₃CCl₃ in the stratosphere. The balloon-borne measurements cover the altitude range of upper troposphere (~8 km in the mid-high latitudes and ~10 km in the tropics) up to the stratosphere (up to ~35 km). We also use CH₃CCl₃ observations from the National Aeronautics and Space Administration (NASA) operated high-altitude, atmospheric-sensing platforms on ER-2 aircrafts. During 1994–2000, NASA conducted several aircraft campaigns to probe the ozone hole formation and recovery by improving our understanding of chemistry, dynamics, and radiation in the upper troposphere and lower stratosphere (UT/LS) region. The measurements of CH₃CCl₃ are conducted by NOAA using the four-channel Airborne Chromatograph for Atmospheric Trace

Table 1
List of AGAGE and NOAA Measurement Sites Used in This analysis, Along With Their Locations, Sampling Altitudes, and Periods of Operation

Sl no.	Site name	Latitude	Longitude	Altitude, m asl (agl) ^a	Data provider	Start of record
1	Mace Head (MHD)	53.33	−9.9	25	AGAGE	1978-
2	Trinidad Head (THD)	41.05	−124.15	140	AGAGE	1980-
3	Barbados (RPB)	13.17	−59.43	42	AGAGE	1978-
4	Samoa (SMO)	−14.23	−170.57	77	AGAGE	1978-
5	Cape Grim (CGO)	−40.68	144.68	164 (70)	AGAGE	1978-
1	Alert (ALT)	82.45	−62.52	210	NOAA	1992-
2	Pt. Barrow (BRW)	73.32	−156.6	8	NOAA	1992-
3	Summit (SUM)	72.58	−38.48	3,200	NOAA	2004-
4	Wisconsin (LEF)	45.93	−90.27	868 (396)	NOAA	1996-
5	THD	41.05	−124.15	120	NOAA	2002-
6	Niwot Ridge (NWR)	40.03	−105.57	3,475	NOAA	1992-
7	Mauna Loa (MLO)	19.54	−155.58	3,397	NOAA	1992-
8	Kumukahi (KUM)	19.52	−154.82	3	NOAA	1996-
9	SMO	−14.23	−170.57	77	NOAA	1992-
10	CGO	−40.68	144.68	164 (70)	NOAA	1992-
11	Palmer station (PSA)	−64.77	−64.05	10	NOAA	1997-
12	South Pole (SPO)	−89.99	−24.8	2,837	NOAA	1992-
Not used ^b	Harvard forest (HFM)	–	–	–	NOAA	1995-
Not used ^b	MHD	–	–	–	NOAA	1998-

Abbreviations: AGAGE, Advanced Global Atmospheric Gases Experiment; NOAA, National Oceanic and Atmospheric Administration.

^aFor sampling altitude, height in meter above sea-level (asl) are given and, when available, also the inlet above ground level height (agl) in parenthesis. ^bNOAA measurements at MHD and HFM are excluded from this analysis. For MHD, we use continuous AGAGE data, and for HFM, the large variabilities observed in CH₃CCl₃ are poorly simulated by ACTM, especially in the early period with high emissions.

Species (ACATS-IV) during the Antarctic Southern Hemisphere Ozone Experiment (ASHOE), the Stratospheric Tracers of Atmospheric Transport (STRAT), the Photochemistry of Ozone Loss in the Arctic Region In Summer (POLARIS) and the SAGE III Ozone Loss and Validation Experiment (SOLVE) (Elkins et al., 1996; Romashkin et al., 2001).

The model simulations are sampled at the nearest model grid for each measurement location (Table 1) within half-an-hour of the actual sampling time. From the observations and the cosampled model values, we calculated monthly and annual-means that are used in the analysis. Both the measurements and model simulations are expressed in units of dry air mole fraction (pmol mol^{−1}; parts-per-trillion, ppt).

2.5. Indirect Estimation of Tropospheric OH

We have indirectly inferred mean tropospheric OH anomalies from the CH₃CCl₃ model-observation differences. As will be shown, the model simulations account for the main drivers (emissions, transport, sinks) of the observed CH₃CCl₃ time series. Note also that about 10% of CH₃CCl₃ is lost in the stratosphere, which is assumed to be modeled well (details in Section 3.2). Remaining model-observation differences are assumed to be caused by either inaccuracy in the applied emissions or by variations in OH. To test the latter, we start from the budget equation of the global CH₃CCl₃ burden and its time variation:

$$\frac{dB}{dt} = E - \frac{B}{\tau} \quad (1)$$

where B is the burden, E are the emissions, and τ is the total lifetime of CH₃CCl₃ ($\tau = 1/(k_{OH} \times [OH] + k_{Cl} \times [Cl] + J)$). Throughout this study, we use observations and model results at monthly mean time intervals for the calculations.

Knowing CH_3CCl_3 emissions, burden, and the burden change in time, we can derive the inverse tropospheric lifetime of CH_3CCl_3 toward loss by OH (K_G , given the assumption that other loss frequencies remain constant over time), which is proportional global tropospheric mean OH (Montzka et al., 2011),

$$K_G = \frac{1}{\tau} = \frac{E}{B} - \frac{dB}{B dt} \quad (2)$$

Note that modeled K_G values, even with constant OH concentrations, may vary in time due to “physical” climate variations, associated with variations in transport and atmospheric temperature, and include the losses in the stratosphere by reaction with Cl radicals and photolysis. The physical K_G variability ($=1/\tau$) can be calculated from the 3-D model simulation in which [OH], [Cl], and photolysis are held constant from year-to-year. To separate this variability from variations caused by “chemical” factors such as variations in the OH abundance driven by its chemical sources and sinks, or wrongly represented CH_3CCl_3 emissions, we estimate anomalies in K_G . To this end, we compare modeled time series to observations at individual time stations. Given observations and model estimates of B and dB/dt , anomalies in K_G are defined as:

$$\Delta K_G = E \left[\frac{1}{B_{\text{obs}}} - \frac{1}{B_{\text{mod}}} \right] - \left[\left\| \frac{dB_{\text{obs}}}{dt} \right\| - \left\| \frac{dB_{\text{mod}}}{dt} \right\| \right] \quad (3)$$

Here the subscripts “obs” and “mod” refer to observations and the model-based parameters, respectively. Alternatively, we may derive emission anomalies as:

$$\Delta E = \frac{d[B_{\text{obs}} - B_{\text{mod}}]}{dt} + \frac{[B_{\text{obs}} - B_{\text{mod}}]}{\tau} \quad (4)$$

To relate modeled and observed mole fractions (in ppt) to global burdens (B , in Gg), we use a factor of 23.65 ± 0.07 Gg ppt⁻¹ (mean and 1- σ standard deviation during 1985–2018). This factor represents the 1981–2018 mean (and 1- σ standard deviation) of the yearly averaged modeled global CH_3CCl_3 burden over the modeled global mean mole fraction (mass-weighted). We have calculated K_G anomalies separately for measurements from each of the AGAGE and NOAA sites before calculating the averages and 1- σ standard deviations for a set of sites. In contrast to box model studies, this approach accounts for spatially resolved emissions and loss processes, as well as for interannually varying transport.

To further investigate drivers of physical K_G variability (Section 3.3), we have performed additional MIROC4-ACTM simulations. In these simulations, we sequentially fix various drivers of variability: MCF emission, transport, and temperature. We fix the emissions to the year 1984 and temperature and transport to climate-driver data for the year 2010. The simulation with 1984 emissions and 2010 transport and temperature is expected to show negligible “physical” K_G variability, since only interannually varying sea-surface temperature is accounted for, which is “overruled” by nudging the simulation to 2010 transport and/or temperature.

3. Results and Discussion

3.1. Global CH_3CCl_3 Distributions in the Simulations

To illustrate the changes in global CH_3CCl_3 , Figure 2 shows the January and July latitude-pressure distribution simulated for two specific years: (1) 1990, when the global total emissions were at their peak (~ 650 Gg year⁻¹) and tropospheric mole fractions were everywhere larger than 100 ppt (top row), and (2) 2005, when the emissions had reduced substantially (~ 25 Gg year⁻¹) and mole fractions had fallen below 25 ppt (bottom row). In the 1990s, the distribution was dominated by transport in the upper troposphere from the NH, where emissions dominate, toward the SH. The tropical transport barrier due to the intertropical convergence zone (ITCZ) is stronger in January and weakens due to the South Asian monsoon in July (Figures 2a and 2b). The situation changed dramatically by 2005 (Figures 2c and 2d), when emissions had become a small term in the global CH_3CCl_3 mass balance equation (Equation 1) (Montzka et al., 2011). By that time, removal by OH in the tropical troposphere had become the dominant term in the global CH_3CCl_3 budget. Removal by OH is evident from the local minimum that is simulated in the tropics, which migrates seasonally from the SH to the NH following the maximum in solar intensity (Figures 2c and 2d). Based on the calculations in MIROC4-ACTM, the local lifetime of CH_3CCl_3 varies

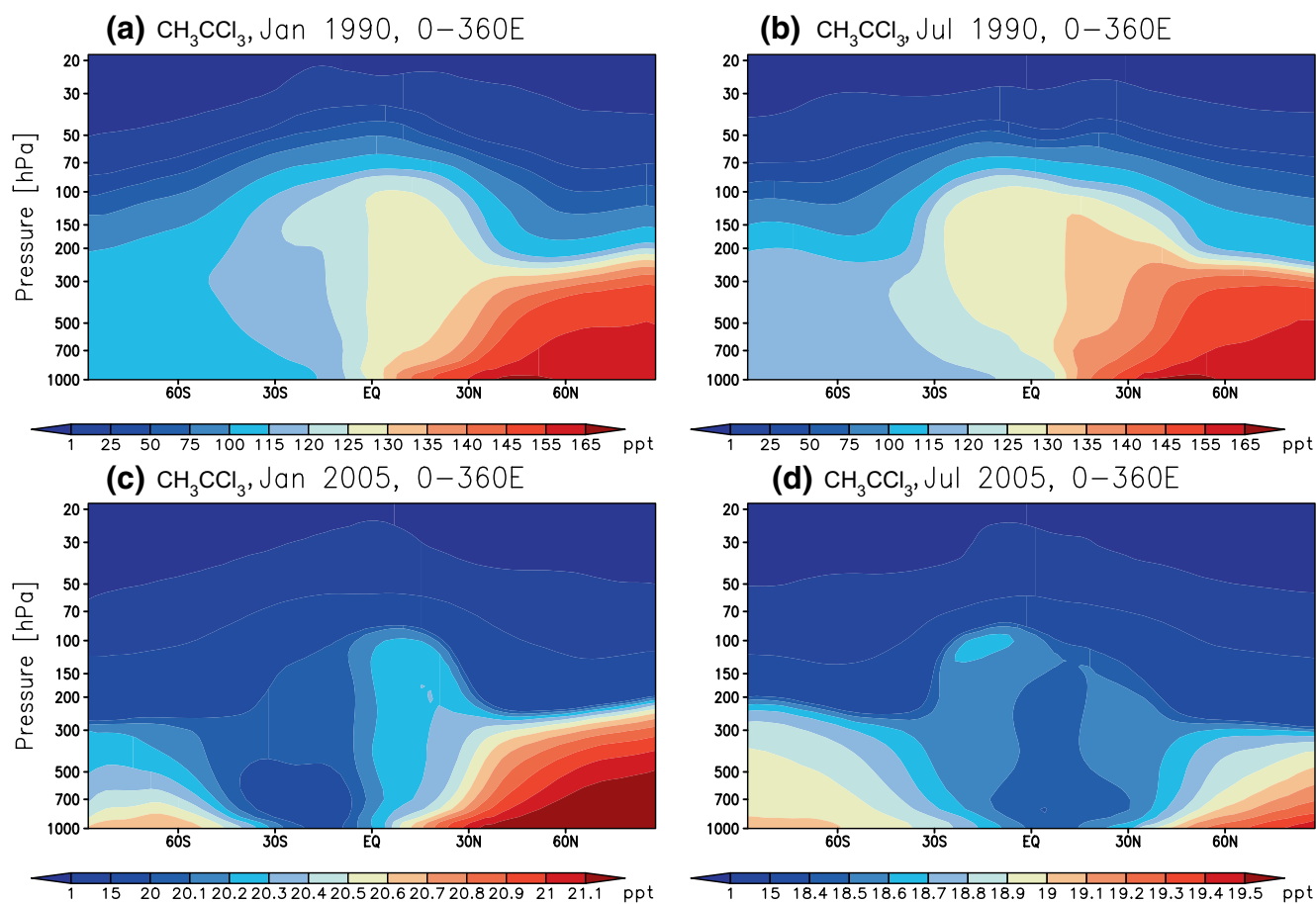


Figure 2. Latitude-pressure distribution of zonal mean CH_3CCl_3 during NH winter (left column) and NH summer (right column) simulated by MIROC4-ACTM for 1990 (top row) and 2005 (bottom row), respectively (simulation PP-OC-c). Note that different color scales are used due to the rapidly changing concentrations of CH_3CCl_3 , that is, a common scale for January and July 2005 would not clearly depict the horizontal and vertical gradients in the troposphere.

from about 3 months in the tropical lower troposphere to 7 years in the tropical upper troposphere (~ 200 mb) and at 60° latitude near the Earth's surface in the model.

3.2. Evaluation of CH_3CCl_3 Simulation in the Upper Troposphere and Stratosphere

About 10% of CH_3CCl_3 is lost to the stratosphere, and the loss budget of CH_3CCl_3 toward the stratosphere primarily depends on stratosphere-troposphere exchange. To validate the ability of the model to simulate the vertical gradient of CH_3CCl_3 in the stratosphere, Figure 3 shows the comparisons of observed and simulated CH_3CCl_3 vertical profiles in the stratosphere. Uncalibrated observations from Hyderabad, India (17.5°N , 78.6°E) in March 1990 are scaled by 0.787 to match the simulated concentration, averaged over March 1990, at 10 km which represents tropospheric air (Lal et al., 1994). Similarly, the reference CH_3CCl_3 profile from Gap, France (44.6°N , 6.1°E), representative of June 1987, is also scaled by 0.855 to match the simulated tropospheric concentration at 8 km (Fabian et al., 1996). The simulated concentrations for Hyderabad match with the observed value of 112 ppt within 13% at 19 km (lower stratosphere). The tropopause height was observed at 16.5 km during the balloon flight. The observed and simulated profiles match better below 19 km (within 4%), and major difference are seen in the altitude range 20–25 km (Figure 3a). Good agreement is also seen for the altitude (26–27 km) at which CH_3CCl_3 observations hit the detection limit and simulated concentrations diminish. The observation-based reference profile and simulation show excellent agreement at all heights over Gap, France (Figure 3b).

To further evaluate the model simulations in the upper troposphere and stratosphere region, we have compared the simulated concentrations along the flight tracks of 4 NASA aircraft campaigns from 1994 to 2000 (Figure 4). Figure 4a shows that the model simulated concentrations closely follow the concentration changes at different

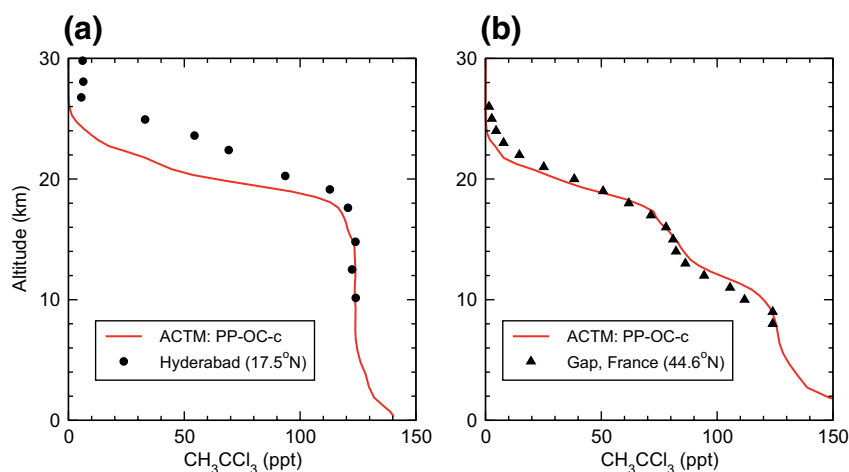


Figure 3. Comparisons of MIROC4-ACTM simulated CH_3CCl_3 vertical profiles with those (a) observed at Hyderabad, India in March 1990 (Lal et al., 1994) (Table S2) and (b) constructed for Gap, France in June 1987 (Fabian et al., 1996) (Table S2). The values from the two sites are scaled to model values in the troposphere, because the aim of this analysis is to validate CH_3CCl_3 vertical gradients in the stratosphere.

latitude and heights (low values correspond to the stratosphere, mostly at around 18–20 km, and high values correspond to the middle and upper troposphere of 5–10 or 15 km, depending on the latitude). Quite a few of the ASHOE flights and all of the STRAT flights were operated in the tropical latitudes, and thus CH_3CCl_3 concentrations typical of the troposphere are measured up to ~ 16 km. For the POLARIS and SOLVE flights, concentrations started to decrease significantly above ~ 10 km (Figure 4c). Figure 4b showed good agreement between the model and observed CH_3CCl_3 for each flight (correlation coefficients, r , greater than 0.93).

Based on the comparisons of the model simulations using balloon and aircraft observations, we conclude that stratospheric-tropospheric exchange and the loss of CH_3CCl_3 in the stratosphere is realistically modeled in ACTM, and proceed with analyzing the tropospheric CH_3CCl_3 budget and the impact of tropospheric OH on this budget.

3.3. Time Evolution of CH_3CCl_3 mole Fractions, Lifetime, and Derived OH Variability

Figure 5 shows that the MIROC4-ACTM simulations, with constant OH, reproduce the CH_3CCl_3 mole fractions at Cape Grim (CGO; 41°S , 145°E) well within 10% (results for the other AGAGE stations are presented in Figure S3). The best agreement is obtained with simulation PP-OC-c (Figure 5b), in which the ocean sink is included and post-2014 emissions are almost constant. We suggest that the inclusion of the oceanic sink, calculated in an earth-system model (Wennberg et al., 2004), is responsible for the improvements compared to our earlier modeling studies (Patra et al., 2014). These improvements are evident from the systematically smaller model-observation differences during 1985–2005 in the simulations that include the ocean sink (PP-OC cases). In other words, if the oceanic sink is neglected, we would need systematically greater OH (or lower CH_3CCl_3 emissions) in the second half of the 1980s and that the OH had to decrease until about the middle of the 1990s, also evident in an earlier study (Bousquet et al., 2005).

The exact decline of the emissions since 2001, however, remains uncertain because no inventory-based emission estimates are available. The overall tendency of simulations to underestimate observed mole fractions after 2015 points to underestimated emissions (Rigby et al., 2017). We therefore test the impact of a slower decline in emissions after 2001 with the PP-OC-7.5 years emission scenario, which results in a positive model-observation differences in CH_3CCl_3 after 2010 (Figure 5b) and a persistent positive K_G anomaly for 2010–2014.

As argued above, the modeled K_G may vary in time due to “physical” climate variations, associated with variations in transport and atmospheric temperature, or due to “chemical factors” such as changes in OH or wrongly represented CH_3CCl_3 emissions. To separate the “physical” and “chemical” variability, we estimate anomalies in K_G . When the model-observation differences at CGO are projected on global K_G anomalies (Equation 3, Figure 5c), values range within $\pm 8\%$ (1998–2018 standard deviation of annual means in Figure 5c amounts to

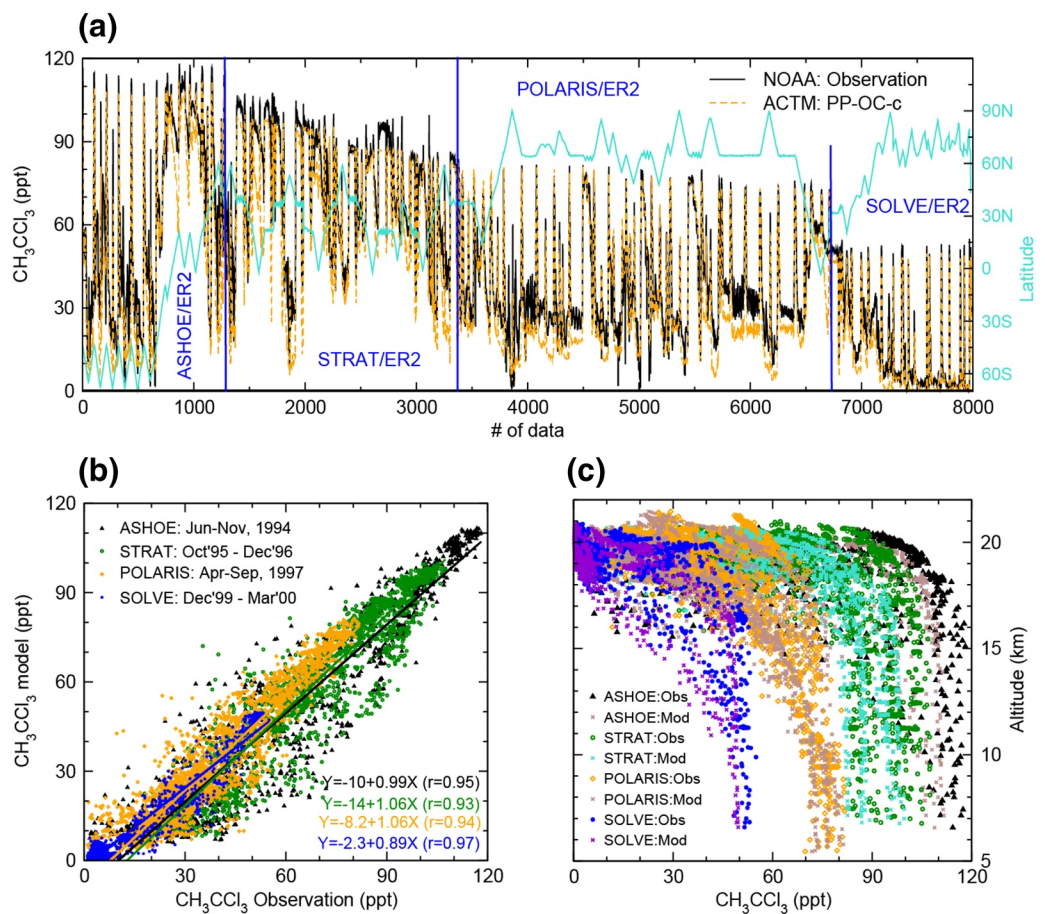


Figure 4. Comparisons of CH₃CCl₃ measurements and model in the UT/LS region. Measurements by NOAA were made by the ACATS-IV instrument onboard ER-2 aircraft campaigns (ASHOE, STRAT, POLARIS, and SOLVE). Panel (a) (top) shows the data for all four campaigns and latitude of flight operation. Panel (b) (bottom-left) shows the statistical significance of the model-observation agreements. Panel (c) (bottom-right) shows the vertical distributions of CH₃CCl₃ as observed and modeled. ACATS-IV, Airborne Chromatograph for Atmospheric Trace Species; ASHOE, Antarctic Southern Hemisphere Ozone Experiment; NOAA, National Oceanic and Atmospheric Administration; POLARIS, Photochemistry of Ozone Loss in the Arctic Region In Summer; SOLVE, SAGE III Ozone Loss and Validation Experiment; STRAT, Stratospheric Tracers of Atmospheric Transport.

3.7%) of the mean K_G of 0.198 year^{-1} (equivalent to mean CH₃CCl₃ lifetime of 5.05 ± 0.10 years) for the control emission case (PP-OC-c). Note that the PP-OC-7.5 years scenario with higher emissions, leads to a positive deviation in the calculated K_G anomalies (Figure 5c), but interannual variations remain robust. This indicates that emissions remain a critical factor in assessing K_G , and [OH], trends. Before 1998, uncertainties in emissions render the projection of model-observation mismatches on K_G less reliable (Montzka et al., 2011). K_G variations in the most recent years (2015 onwards) may also be less reliable, due to the small atmospheric CH₃CCl₃ burden, instrumental issues related to accurately measuring small atmospheric mole fractions, and uncertainty in remaining emissions.

The K_G anomalies are superimposed on the MIROC4-ACTM's internal "physical" IAVs and trend, which shows a ~3% increase in K_G over the past ~30 years (black line in Figure 5d). This corresponds to a lifetime decrease from 5.11 ± 0.10 years during 1986–1996 to 4.95 ± 0.10 years during 2009–2018. Variations in annual mean K_G in this simulation are on the order of 1%, for instance during the El-Niño and La-Niña events around 1998 and 2010, respectively (the ENSO and K_G variability is further addressed in Section 3.4). The systematic increase in physical K_G ($0.80\% \text{ decade}^{-1}$ in the period 1985–2018) is caused (1) by changes in the rate of stratosphere-troposphere exchange of CH₃CCl₃ due the modifications in latitude-height gradients with time (see Figure 2), (2) by increases in temperature-dependent loss rates, and (3) by trends in transport processes that bring CH₃CCl₃ to its

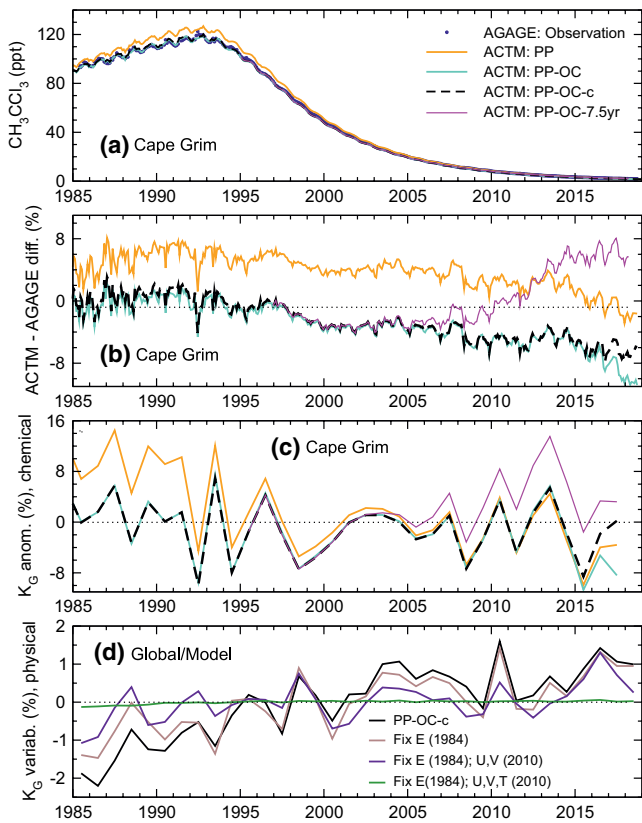


Figure 5. (a) Time series of monthly mean simulated mole fractions and AGAGE observations of CH_3CCl_3 for the period 1981–2018 at Cape Grim Observatory (CGO; 41°S , 145°E). Panel (b) shows the monthly model—observation differences at CGO, and in panel (c), the inferred yearly “chemical” K_G anomalies using CGO data are shown. Panel (d) presents the “physical” model-calculated K_G variations (Equation 2) in black. The brown, purple, and green lines are derived from simulations with respectively constant 1984 emissions, constant 1984 emissions (E) and climatological 2010 horizontal winds (U, V), and constant 1984 emissions (E) and climatological 2010 winds and temperature (U, V, T). AGAGE, Advanced Global Atmospheric Gases Experiment.

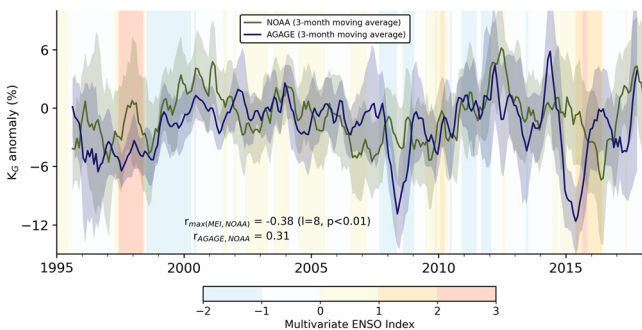


Figure 6. Time series of monthly K_G anomalies, estimated by combining AGAGE and NOAA measurement sites, with $1\text{-}\sigma$ standard deviations shown by shading. The shaded bars in the background represent the multivariate ENSO index, version 2 (MEI.v2) (Wolter & Timlin, 2011). AGAGE, Advanced Global Atmospheric Gases Experiment; ENSO, El Niño Southern Oscillation; NOAA, National Oceanic and Atmospheric Administration.

main sink area in the tropics (Naus et al., 2019). The effect of the changing global CH_3CCl_3 distribution on K_G is assessed by a simulation with constant 1984 emissions (Fix E case in Figure 5d, 0.55% decade $^{-1}$ increase in K_G). This simulation results in a steady state CH_3CCl_3 distribution, with lifetime variations driven solely by temperature and transport variations. The effects of transport and temperature are assessed separately by nudging the winds (purple line, 0.035% decade $^{-1}$ increase in K_G) and winds and temperature (green line, 0.25% decade $^{-1}$ increase in K_G) repeatedly to meteorological driver data of 2010. This shows a dominant role for the temperature in driving both the trend and interannual variations of K_G .

We found that the model-observation CH_3CCl_3 differences produce highly consistent variations across all AGAGE stations (Figure S3), which points to a common global driver. As a test for the interannual transport simulated by MIROC4-ACTM, we compared the meridional gradients in sulfur hexafluoride (SF_6) measured at CGO and eight other sites located north of CGO measured by NOAA (Figure S1). The model and observed gradients show statistically significant correlation coefficients, 0.62 or greater for seven out of eight sites. Slightly lower correlation coefficients (0.38) for the Ascension Island (ASC)-CGO differences may arise from the coarse spatial resolution of the model (T42) or uncertainties in the emission distribution or precision of the measurement (~ 0.04 ppt for the NOAA flask measurements). Because the other terms in the CH_3CCl_3 budget are not likely to exhibit strong interannual variations, it seems justified to assign these mismatches to “chemical” K_G variations, caused by OH changes.

3.4. Trends and Anomalies in Global Mean K_G

Figure 6 depicts the global monthly K_G anomalies from the PP-OC-c scenario as derived by separately averaging K_G data from either 5 AGAGE (Prinn et al., 2018) or 12 NOAA (Montzka et al., 2011) sites (Table 1). The corresponding emission anomalies derived using Equation 4 are presented in Figure S4. The NOAA and AGAGE monthly values represent the arithmetic mean of the individual stations' estimates, and co-vary in time with a Pearson's moment correlation coefficient of $r = 0.31$ (Figure 6), suggesting a robust estimation of K_G anomalies from these independent measurements. Larger differences between the networks in 2007–2008 and 2014–2015 are not well understood. Both networks agree on positive K_G anomalies during 2000–2005 and around 2012, and on the absence of a significant long-term trend during 2000–2014 in the PP-OC-c emission scenario. A similar analysis but for CH_3CCl_3 decay rate anomaly was performed by Holmes et al. (2013), where they reported a systematic offset between the two networks during 1998–2001, a period when emissions are still significant for northern-southern hemisphere differences in CH_3CCl_3 . We suspect their results are an artifact of not accounting for the differences in the observational network, which is minimized here by taking model-observation differences.

Since, K_G is mainly proportional to global mean OH abundance, we compare our results of K_G anomalies with OH anomalies from the published literature. The annual K_G variability estimated here (2.08% for NOAA and 2.67% for AGAGE during 1996–2015) is only slightly lower than the box-model estimates reported as 2.98% by Turner et al. (2017) and 3.04% by Rigby et al. (2017), or 2.3% by Montzka et al. (2011) over a shorter period of

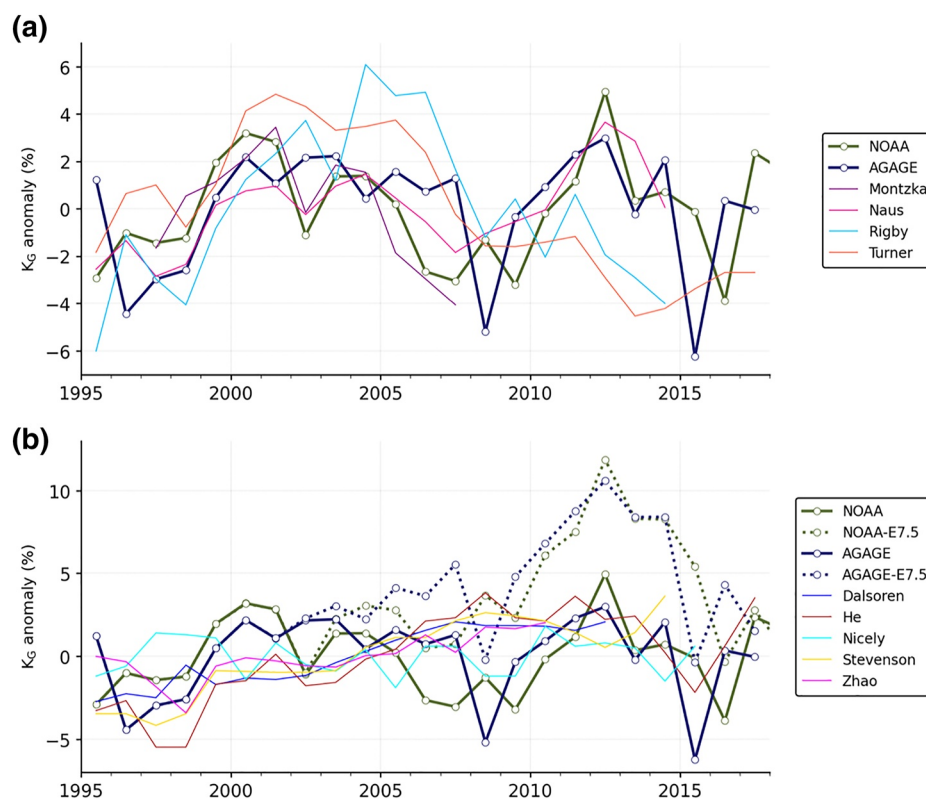


Figure 7. (a, upper panel) Comparisons between annual mean K_G anomalies from this work and similar analyses using box models (Montzka et al., 2011; Turner et al., 2017; Rigby et al., 2017; Naus et al., 2019). (b, lower panel) Simulated OH variations using various CTMs (Dalsøren et al., 2016; He et al., 2020; Nicely et al., 2018) or CTM ensembles (Stevenson et al., 2020; Zhao et al., 2020). K_G variations in these model simulations are sometimes weighted by the T -dependent rate constant of the $\text{CH}_4 + \text{OH}$ reaction, which has comparable T -dependence as the $\text{CH}_3\text{CCl}_3 + \text{OH}$ reaction. For comparison with calculated trends, also results from the scenario PP-OC-7.5 years are shown.

1998–2007. This is in line with our finding that “chemical” drivers (Figure 5c) dominate over “physical” drivers (Figure 5d) of K_G variability at any given decade since 1985.

The derived K_G anomalies anticorrelate with ENSO (to $r \sim -0.29$ when shifted by 3 months and to a maximum of $r = -0.38$ when shifted by 8 months), and high and low K_G 's are associated with the La Niña and El Niño phases (Figure 6). A temporal delay in the K_G anomaly is not unreasonable, since ENSO-driven fire emission anomalies from drought-affected subcontinents are delayed by 2–5 months with respect to the ENSO index (Patra et al., 2005) (see also Figure S5 for the region of ENSO related emissions and duration of emissions). The increased emissions in carbon monoxide (CO) and nitrogen oxides (NO_x) and volatile organic compounds (VOCs) affect the OH variability similarly, an instant reduction in OH by first-order reactions (Gaubert et al., 2017; Holmes et al., 2013; Nguyen et al., 2020; Stevenson et al., 2020). It has been proposed that elevated OH during La Niña is caused by increased convection and lightning in the tropics (Turner et al., 2018). However, no process-based chemistry-transport model re-produces this variability at interannual time scales, as has been derived from CH_3CCl_3 time series here. Low OH inferred during strong El Niño phases has been attributed to increased tropical cloud cover (shielding UV below clouds) and OH-reduction by CO from global wildfires (Prinn et al., 2001, 2005). Recent analysis of CTM results confirms the (negative) link between ENSO and OH (Rowlinson et al., 2019; Zhao et al., 2020).

Figure 7 compares our results of the K_G anomaly with results from various CH_3CCl_3 global analyses using box model approaches (Montzka et al., 2011; Naus et al., 2019; Rigby et al., 2017; Turner et al., 2017). We notice broad consistency in derived K_G variations, specifically from studies using NOAA observations as the single data source (Montzka et al., 2011; Naus et al., 2019). Variations derived by two other studies deviate more from our results, specifically after 2010 (Rigby et al., 2017; Turner et al., 2017). As outlined in Naus et al. (2019), these

deviations might be caused by the inability of box models to account for the changing global CH_3CCl_3 distribution. Likely also the choices of observational and model errors in these studies play an important role. Our new results for K_G variability using a detailed 3D transport model exploit the information of the measurement networks to its full extent by accounting for transport variability and changes in the global CH_3CCl_3 distribution. Our results do not confirm the OH decline for the 2010–2015 period that was a potential conclusion from box model studies (Rigby et al., 2017; Turner et al., 2017).

When we compare our results to modeling efforts to quantify OH variability and trends using full CTMs in Figure 7b (Dalsøren et al., 2016; He et al., 2020; Stevenson et al., 2020), few similarities are found. Note that our derived long-term K_G trend strongly depends on assumed CH_3CCl_3 emission declines after 2001, as shown by the results from the PP-OC-7.5 years scenarios. Changing the assumed emission decay time constant from 5 to 7.5 years leads to a 10% K_G increase in the 2002–2012 period (Figure 7b). Most models, except one that is based on a machine learning technique (Nicely et al., 2018), derive positive OH trends of roughly 3% decade⁻¹ during 1995–2017. Note that the no OH trend in Nicely et al. (2018), similar to our trends, are “chemical,” since physical changes, which are dominated by temperature changes (Figure 5d), are accounted for by the CTMs. Chemical drivers of the OH long-term trend in modeling studies have been identified as the net effect of changing emissions and concentrations of near-term climate forcers, for example, decreases in CO and increases in NO_x emissions (Stevenson et al., 2020). At the same time, however, key drivers of OH variabilities show the largest model diversity (Wild et al., 2020).

Differences between the networks do not lead to different conclusions concerning the small long-term trend in K_G . This trend, which is important for assessing the global methane budget, is critically sensitive to the CH_3CCl_3 emission history. We found that, even if we assume a slower decay in emissions, sustained positive K_G anomalies after 2015 are not supported by recent observations. Reemission of CH_3CCl_3 previously dissolved into the oceans (Wennberg et al., 2004) might play a role, but this needs experimental confirmation and continued precise measurements of the global atmospheric CH_3CCl_3 decay rate in future years.

4. Conclusions

We have conducted simulations of CH_3CCl_3 during the period of 1985–2018 using the MIROC4-ACTM to estimate the variability in tropospheric OH. Four different emission scenarios were used to test how sensitive the model simulations are to these scenarios, and how well the observed CH_3CCl_3 time series from 13 global sites from two different observational networks, namely, the AGAGE continuous on-site and NOAA flask sampling networks, are reproduced. The model simulations for the upper troposphere and stratosphere height regions are validated using balloon-borne cryo-sampling observations and a series of NASA aircraft experiments. We derived K_G variability using independent observations from both the CH_3CCl_3 observation networks from 1998 to 2018. Our major conclusions are:

1. Model simulations show contrasting latitude-pressure distribution of CH_3CCl_3 in the period of high emissions and low emissions. The model simulations reproduce the concentration gradients in the upper troposphere and stratospheric altitudes observed during balloon and aircraft measurements well, suggesting that model transport and CH_3CCl_3 losses are well parameterized
2. The best overall agreement with the AGAGE measured time series is produced by the model simulations using the emission scenario that includes the oceanic sink (most significant in the period 1985–1995) and an emission decrease at a decay constant of 5 years during the period 2001–2019
3. Derived K_G anomalies from the model-observation differences show consistent features using both AGAGE or NOAA data during most years. This internetwork consistency is obtained because the model-observation differences are found to be similar for all sites because the intersite gradients are simulated well by the model
4. The K_G anomalies are separated into two components, physical (changes in temperature dependent reaction rate, stratosphere-troposphere exchange etc.) and chemical (OH abundance change). The physical component caused only a small portion of the total interannual variability derived for K_G (~2.3%), but also showed systematic increase at a rate of 0.80% decade⁻¹ during the 1985–2018 period, predominantly because of secular increases in temperature
5. Interannual variations in chemical K_G anomaly are related in part to ENSO variability, a decrease in OH during the El Niño phase and an increase in the La Niña phase is observed. Our detailed analysis suggests no significant trends in this K_G anomaly (and therefore [OH]) during the 1996–2017 period

Data Availability Statement

NOAA flask data from their cooperative network are available for download from <https://www.esrl.noaa.gov/gmd/hats/>. AGAGE data are available from <http://agage.mit.edu/data> (incl. guidelines for use of AGAGE data) and ESS-DIVE website <http://cdiac.ess-dive.lbl.gov/ndps/alegage.html>.

Acknowledgments

CH₃CCl₃ measurements continue to clarify more of the long-lasting uncertainties in OH variability and trends, thanks to the dedicated efforts by our colleagues contributing to the AGAGE and NOAA measurement programs. The Mace Head, Trinidad Head, Ragged Point, Cape Matatula, and Cape Grim AGAGE stations are supported by the National Aeronautics and Space Administration (NASA) (grants NNX16AC98G to MIT, and NNX16AC97G and NNX16AC96G to SIO). Support also comes from the UK Department for Business, Energy & Industrial Strategy (BEIS) for Mace Head, the National Oceanic and Atmospheric Administration (NOAA) for Barbados, and the Commonwealth Scientific and Industrial Research Organization (CSIRO) and the Bureau of Meteorology (Australia) for Cape Grim. The balloon-borne measurements at Hyderabad were conducted by a collaborative project between the Max-Planck Institute of Aeronomy, Lindau and Indian Space Research Organisation (ISRO), Bangalore. Data archive: <http://agage.mit.edu/data>. M. Krol received funding from the European Research Council (ERC) under the European Union's Horizon 2020 research and innovation program under grant agreement No 742798. S. Naus is supported by NWO (grant 824.15.002). This study is partly supported by the Arctic Challenge for Sustainability II grant (JPMXD1420318865) of the Ministry of Education, Science, Culture and Sports (MEXT), Japan; the Environment Research and Technology Development Fund (JPMEERF20182002) of the Environmental Restoration and Conservation Agency of Japan.

References

- Arnold, T., Mühle, J., Salameh, P. K., Harth, C. M., Ivy, D. J., & Weiss, R. F. (2012). Automated measurement of nitrogen trifluoride in ambient air. *Analytical Chemistry*, 84(11), 4798–4804. <https://doi.org/10.1021/ac300373e>
- Bousquet, P., Hauglustaine, D. A., Peylin, P., Carouge, C., & Ciais, P. (2005). Two decades of OH variability as inferred by an inversion of atmospheric transport and chemistry of methyl chloroform. *Atmospheric Chemistry and Physics*, 5(10), 2635–2656. <https://doi.org/10.5194/acp-5-2635-2005>
- Brenninkmeijer, C. A. M., Manning, M. R., Lowe, D. C., Wallace, G., Sparks, R. J., & Volz-Thomas, A. (1992). Interhemispheric asymmetry in OH abundance inferred from measurements of atmospheric 14CO. *Nature*, 356(6364), 50–52. <https://doi.org/10.1038/356050a0>
- Burkholder, J. B., Sander, S. P., Abbatt, J., Barker, J. R., Huie, R. E., Kolb, C. E., et al. (2015). *Chemical kinetics and photochemical data for use in atmospheric studies: Evaluation no. 18*. Pasadena, CA: Jet Propulsion Laboratory, National Aeronautics and Space Administration. <http://hdl.handle.net/2014/45510>
- Butler, J. H., Elkins, J. W., Thompson, T. M., Hall, B. D., Swanson, T. H., & Koropalov, V. (1991). Oceanic consumption of CH₃ CCl₃: Implications for tropospheric OH. *Journal of Geophysical Research*, 96(D12), 22347. <https://doi.org/10.1029/91JD02126>
- Crutzen, P. J., & Zimmermann, P. H. (1991). The changing photochemistry of the troposphere. *Tellus A: Dynamic Meteorology and Oceanography*, 43(4), 136–151. <https://doi.org/10.3402/tellusa.v43i4.11943>
- Dalsøren, S. B., Myhre, C. L., Myhre, G., Gomez-Pelaez, A. J., Søvde, O. A., Isaksen, I. S. A., et al. (2016). Atmospheric methane evolution the last 40 years. *Atmospheric Chemistry and Physics*, 16(5), 3099–3126. <https://doi.org/10.5194/acp-16-3099-2016>
- Elkins, J. W., Fahey, D. W., Gilligan, J. M., Dutton, G. S., Baring, T. J., Volk, C. M., et al. (1996). Airborne gas chromatograph for in situ measurements of long-lived species in the upper troposphere and lower stratosphere. *Geophysical Research Letters*, 23(4), 347–350. <https://doi.org/10.1029/96GL00244>
- Fabian, P., Borchers, R., Leifer, R., Subbaraya, B. H., Lal, S., & Boy, M. (1996). Global stratospheric distribution of halocarbons. *Atmospheric Environment*, 30(10–11), 1787–1796. [https://doi.org/10.1016/1352-2310\(95\)00387-8](https://doi.org/10.1016/1352-2310(95)00387-8)
- Francey, R. J., Frederiksen, J. S., Paul Steele, L., & Langenfelds, R. L. (2019). Variability in a four-network composite of atmospheric CO₂ differences between three primary baseline sites. *Atmospheric Chemistry and Physics*, 19(23), 14741–14754. <https://doi.org/10.5194/acp-19-14741-2019>
- Gaubert, B., Worden, H. M., Arellano, A. F. J., Emmons, L. K., Tilmes, S., Barré, J., et al. (2017). Chemical feedback from decreasing carbon monoxide emissions. *Geophysical Research Letters*, 44(19), 9985–9995. <https://doi.org/10.1002/2017GL074987>
- He, J., Naik, V., Horowitz, L. W., Dlugokencky, E., & Thoning, K. (2020). Investigation of the global methane budget over 1980–2017 using GFDL-AM4.1. *Atmospheric Chemistry and Physics*, 20(2), 805–827. <https://doi.org/10.5194/acp-20-805-2020>
- Holmes, C. D., Prather, M. J., Søvde, O. A., & Myhre, G. (2013). Future methane, hydroxyl, and their uncertainties: Key climate and emission parameters for future predictions. *Atmospheric Chemistry and Physics*, 13(1), 285–302. <https://doi.org/10.5194/acp-13-285-2013>
- Kobayashi, S., Ota, Y., Harada, Y., Ebata, A., Moriya, M., Onoda, H., et al. (2015). The JRA-55 reanalysis: General specifications and basic characteristics. *Journal of the Meteorological Society of Japan*, 93(1), 5–48. <https://doi.org/10.2151/jmsj.2015-001>
- Krol, M. C., & Lelieveld, J. (2003). Can the variability in tropospheric OH be deduced from measurements of 1,1,1-trichloroethane (methyl chloroform)? *Journal of Geophysical Research*, 108(3), 4125. <https://doi.org/10.1029/2002jd002423>
- Krol, M. C., Meirink, J. F., Bergamaschi, P., Mak, J. E., Lowe, D., Jöckel, P., et al. (2008). What can 14CO measurements tell us about OH? *Atmospheric Chemistry and Physics*, 8(16), 5033–5044. <https://doi.org/10.5194/acp-8-5033-2008>
- Lal, S., Borchers, R., Fabian, P., Patra, P. K., & Subbaraya, B. H. (1994). Vertical distribution of methyl bromide over Hyderabad, India. *Tellus B: Chemical and Physical Meteorology*, 46(5), 373–377. <https://doi.org/10.1034/j.1600-0889.1994.t01-3-00003.x>
- Lelieveld, J., Boursoukoudis, E., Brühl, C., Fischer, H., Fuchs, H., Harder, H., et al. (2018). The South Asian monsoon—pollution pump and purifier. *Science*, 361(6399), 270–273. <https://doi.org/10.1126/science.aar2501>
- Lelieveld, J., Peters, W., Dentener, F. J., & Krol, M. C. (2002). Stability of tropospheric hydroxyl chemistry. *Journal of Geophysical Research*, 107(D23), ACH17-1–ACH17-11. <https://doi.org/10.1029/2002JD002272>
- Levy, H. (1971). Normal atmosphere: Large radical and formaldehyde concentrations predicted. *Science*, 173(3992), 141–143. <https://doi.org/10.1126/science.173.3992.141>
- Lovelock, J. E. (1977). Methyl chloroform in the troposphere as an indicator of OH radical abundance. *Nature*, 267(5606), 32. <https://doi.org/10.1038/267032a0>
- Makide, Y., & Rowland, F. S. (1981). Tropospheric concentrations of methylchloroform, CH₃CCl₃, in January 1978 and estimates of the atmospheric residence times for hydrohalocarbons. *Proceedings of the National Academy of Sciences of the United States of America*, 78(10), 5933–5937. <https://doi.org/10.1073/pnas.78.10.5933>
- McCulloch, A., & Midgley, P. (2001). The history of methyl chloroform emissions: 1951–2000. *Atmospheric Environment*, 35(31), 5311–5319. [https://doi.org/10.1016/S1352-2310\(01\)00306-5](https://doi.org/10.1016/S1352-2310(01)00306-5)
- McNorton, J., Chipperfield, M. P., Gloor, M., Wilson, C., Feng, W., Hayman, G. D., et al. (2016). Role of OH variability in the stalling of the global atmospheric CH₄ growth rate from 1999 to 2006. *Atmospheric Chemistry and Physics*, 16(12), 7943–7956. <https://doi.org/10.5194/acp-16-7943-2016>
- Miller, B. R., Weiss, R. F., Salameh, P. K., Tanhua, T., Grealley, B. R., Mühle, J., & Simmonds, P. G. (2008). Medusa: A sample preconcentration and GC/MS detector system for in situ measurements of atmospheric trace halocarbons, hydrocarbons, and sulfur compounds. *Analytical Chemistry*, 80(5), 1536–1545. <https://doi.org/10.1021/ac702084k>
- Montzka, S. A. (2000). New observational constraints for atmospheric hydroxyl on global and hemispheric scales. *Science*, 288(5465), 500–503. <https://doi.org/10.1126/science.288.5465.500>
- Montzka, S. A., Krol, M., Dlugokencky, E., Hall, B., Jöckel, P., & Lelieveld, J. (2011). Small interannual variability of global atmospheric hydroxyl. *Science*, 331(6013), 67–69. <https://doi.org/10.1126/science.1197640>

- Murray, L. T., Mickley, L. J., Kaplan, J. O., Sofen, E. D., Pfeiffer, M., & Alexander, B. (2014). Factors controlling variability in the oxidative capacity of the troposphere since the Last Glacial Maximum. *Atmospheric Chemistry and Physics*, *14*(7), 3589–3622. <https://doi.org/10.5194/acp-14-3589-2014>
- Naik, V., Voulgarakis, A., Fiore, A. M., Horowitz, L. W., Lamarque, J. F., Lin, M., et al. (2013). Preindustrial to present-day changes in tropospheric hydroxyl radical and methane lifetime from the Atmospheric Chemistry and Climate Model Intercomparison Project (ACCMIP). *Atmospheric Chemistry and Physics*, *13*(10), 5277–5298. <https://doi.org/10.5194/acp-13-5277-2013>
- Naus, S., Montzka, S. A., Pandey, S., Basu, S., Dlugokencky, E. J., & Krol, M. (2019). Constraints and biases in a tropospheric two-box model of OH. *Atmospheric Chemistry and Physics*, *19*(1), 407–424. <https://doi.org/10.5194/acp-19-407-2019>
- Naus, S., Montzka, S. A., Patra, P. K., & Krol, M. C. (2020). A 3D-model inversion of methyl chloroform to constrain the atmospheric oxidative capacity. *Atmospheric Chemistry and Physics Discussions*. <https://doi.org/10.5194/acp-2020-624>
- Nguyen, N. H., Turner, A. J., Yin, Y., Prather, M. J., & Frankenberg, C. (2020). Effects of chemical feedbacks on decadal methane emissions estimates. *Geophysical Research Letters*, *47*(3). <https://doi.org/10.1029/2019gl085706>
- Nicely, J. M., Canty, T. P., Manyin, M., Oman, L. D., Salawitch, R. J., Steenrod, S. D., et al. (2018). Changes in global tropospheric OH expected as a result of climate change over the last several decades. *Journal of Geophysical Research: Atmospheres*, *123*(18), 10774–10795. <https://doi.org/10.1029/2018JD028388>
- Nicely, J. M., Duncan, B. N., Hanisco, T. F., Wolfe, G. M., Salawitch, R. J., Deushi, M., et al. (2020). A machine learning examination of hydroxyl radical differences among model simulations for CCM1-1. *Atmospheric Chemistry and Physics*, *20*(3), 1341–1361. <https://doi.org/10.5194/acp-20-1341-2020>
- Patra, P. K., Houweling, S., Krol, M., Bousquet, P., Belikov, D., Bergmann, D., et al. (2011). TransCom model simulations of CH₄ and related species: Linking transport, surface flux and chemical loss with CH₄ variability in the troposphere and lower stratosphere. *Atmospheric Chemistry and Physics*, *11*(24), 12813–12837. <https://doi.org/10.5194/acp-11-12813-2011>
- Patra, P. K., Ishizawa, M., Maksyutov, S., Nakazawa, T., & Inoue, G. (2005). Role of biomass burning and climate anomalies for land-atmosphere carbon fluxes based on inverse modeling of atmospheric CO₂. *Global Biogeochemical Cycles*, *19*(3), GB3005. <https://doi.org/10.1029/2004GB002258>
- Patra, P. K., Krol, M. C., Montzka, S. A., Arnold, T., Atlas, E. L., Lintner, B. R., et al. (2014). Observational evidence for interhemispheric hydroxyl-radical parity. *Nature*, *513*(7517), 219–223. <https://doi.org/10.1038/nature13721>
- Patra, P. K., Takigawa, M., Watanabe, S., Chandra, N., Ishijima, K., & Yamashita, Y. (2018). Improved chemical tracer simulation by MIROC4.0-based atmospheric chemistry-transport model (MIROC4-ACTM). *Scientific Online Letters on the Atmosphere*, *14*, 91–96. <https://doi.org/10.2151/sola.2018-016>
- Prather, M., & Spivakovsky, C. M. (1990). Tropospheric OH and the lifetimes of hydrochlorofluorocarbons. *Journal of Geophysical Research*, *95*(D11), 18723. <https://doi.org/10.1029/JD095iD11p18723>
- Prinn, R. G., Cunnold, D., Simmonds, P., Alyea, F., Boldi, R., Crawford, A., et al. (1992). Global average concentration and trend for hydroxyl radicals deduced from ALE/GAGE trichloroethane (methyl chloroform) data for 1978–1990. *Journal of Geophysical Research*, *97*(D2), 2445. <https://doi.org/10.1029/91JD02755>
- Prinn, R. G., Huang, J., Weiss, R. F., Cunnold, D. M., Fraser, P. J., Simmonds, P. G., et al. (2001). Evidence for substantial variations of atmospheric hydroxyl radicals in the past two decades. *Science*, *292*(5523), 1882–1888. <https://doi.org/10.1126/science.1058673>
- Prinn, R. G., Huang, J., Weiss, R. F., Cunnold, D. M., Fraser, P. J., Simmonds, P. G., et al. (2005). Evidence for variability of atmospheric hydroxyl radicals over the past quarter century. *Geophysical Research Letters*, *32*(7), L07809. <https://doi.org/10.1029/2004GL022228>
- Prinn, R. G., Weiss, R. F., Arduini, J., Arnold, T., DeWitt, H. L., Fraser, P. J., et al. (2018). History of chemically and radiatively important atmospheric gases from the Advanced Global Atmospheric Gases Experiment (AGAGE). *Earth System Science Data*, *10*(2), 985–1018. <https://doi.org/10.5194/essd-10-985-2018>
- Prinn, R. G., Weiss, R. F., Fraser, P. J., Simmonds, P. G., Cunnold, D. M., Alyea, F. N., et al. (2000). A history of chemically and radiatively important gases in air deduced from ALE/GAGE/AGAGE. *Journal of Geophysical Research*, *105*(D14), 17751–17792. <https://doi.org/10.1029/2000JD900141>
- Rigby, M., Montzka, S. A., Prinn, R. G., White, J. W. C., Young, D., O'Doherty, S., et al. (2017). Role of atmospheric oxidation in recent methane growth. *Proceedings of the National Academy of Sciences of the United States of America*, *114*(21), 5373–5377. <https://doi.org/10.1073/pnas.1616426114>
- Romashkin, P. A., Hurst, D. F., Elkins, J. W., Dutton, G. S., Fahey, D. W., Dunn, R. E., et al. (2001). In situ measurements of long-lived trace gases in the lower stratosphere by gas chromatography. *Journal of Atmospheric and Oceanic Technology*, *18*(7), 1195–1204. [https://doi.org/10.1175/1520-0426\(2001\)018<1195:ISMOLL>2.0.CO;2](https://doi.org/10.1175/1520-0426(2001)018<1195:ISMOLL>2.0.CO;2)
- Rowlinson, M. J., Rap, A., Arnold, S. R., Pope, R. J., Chipperfield, M. P., McNorton, J., et al. (2019). Impact of El Niño–Southern Oscillation on the interannual variability of methane and tropospheric ozone. *Atmospheric Chemistry and Physics*, *19*(13), 8669–8686. <https://doi.org/10.5194/acp-19-8669-2019>
- Seinfeld, J. H., & Pandis, S. N. (2006). *Atmospheric chemistry and physics: From air pollution to climate change*. New York, NY: John Wiley & Sons. ISBN: 978-1-118-94740-1.
- Singh, H. B., Kanakidou, M., Crutzen, P. J., & Jacob, D. J. (1995). High concentrations and photochemical fate of oxygenated hydrocarbons in the global troposphere. *Nature*, *378*(6552), 50–54. <https://doi.org/10.1038/378050a0>
- Spivakovsky, C. M., Logan, J. A., Montzka, S. A., Balkanski, Y. J., Foreman-Fowler, M., Jones, D. B. A., et al. (2000). Three-dimensional climatological distribution of tropospheric OH: Update and evaluation. *Journal of Geophysical Research*, *105*(D7), 8931–8980. <https://doi.org/10.1029/1999JD901006>
- Stevenson, D. S., Zhao, A., Naik, V., O'Connor, F. M., Tilmes, S., Zeng, G., et al. (2020). Trends in global tropospheric hydroxyl radical and methane lifetime since 1850 from AerChemMIP. *Atmospheric Chemistry and Physics*, *20*(21), 12905–12920. <https://doi.org/10.5194/acp-20-12905-2020>
- Takahashi, T., Sutherland, S. C., Wanninkhof, R., Sweeney, C., Feely, R. A., Chipman, D. W., et al. (2009). Climatological mean and decadal change in surface ocean pCO₂, and net sea–air CO₂ flux over the global oceans. *Deep Sea Research Part II: Topical Studies in Oceanography*, *56*(8–10), 554–577. <https://doi.org/10.1016/j.dsr2.2008.12.009>
- Takigawa, M., Takahashi, M., & Akiyoshi, H. (1999). Simulation of ozone and other chemical species using a Center for Climate System Research/National Institute for Environmental Studies atmospheric GCM with coupled stratospheric chemistry. *Journal of Geophysical Research*, *104*(D11), 14003–14018. <https://doi.org/10.1029/1998JD100105>
- Turner, A. J., Frankenberg, C., Wennberg, P. O., & Jacob, D. J. (2017). Ambiguity in the causes for decadal trends in atmospheric methane and hydroxyl. *Proceedings of the National Academy of Sciences of the United States of America*, *114*(21), 5367–5372. <https://doi.org/10.1073/pnas.1616020114>

- Turner, A. J., Fung, I., Naik, V., Horowitz, L. W., & Cohen, R. C. (2018). Modulation of hydroxyl variability by ENSO in the absence of external forcing. *Proceedings of the National Academy of Sciences of the United States of America*, *115*(36), 8931–8936. <https://doi.org/10.1073/pnas.1807532115>
- Voulgarakis, A., Naik, V., Lamarque, J.-F., Shindell, D. T., Young, P. J., Prather, M. J., et al. (2013). Analysis of present day and future OH and methane lifetime in the ACCMIP simulations. *Atmospheric Chemistry and Physics*, *13*(5), 2563–2587. <https://doi.org/10.5194/acp-13-2563-2013>
- Watanabe, S., Kawatani, Y., Tomikawa, Y., Miyazaki, K., Takahashi, M., & Sato, K. (2008). General aspects of a T213L256 middle atmosphere general circulation model. *Journal of Geophysical Research*, *113*(12), D12110. <https://doi.org/10.1029/2008JD010026>
- Wells, K. C., Millet, D. B., Payne, V. H., Deventer, M. J., Bates, K. H., de Gouw, J. A., et al. (2020). Satellite isoprene retrievals constrain emissions and atmospheric oxidation. *Nature*, *585*(7824), 225–233. <https://doi.org/10.1038/s41586-020-2664-3>
- Wennberg, P. O., Peacock, S., Randerson, J. T., & Bleck, R. (2004). Recent changes in the air-sea gas exchange of methyl chloroform. *Geophysical Research Letters*, *31*(16), L16112. <https://doi.org/10.1029/2004GL020476>
- Wild, O., Voulgarakis, A., O’Apos, Connor, F., Lamarque, J.-F., Ryan, E. M., & Lee, L. (2020). Global sensitivity analysis of chemistry-climate model budgets of tropospheric ozone and OH: Exploring model diversity. *Atmospheric Chemistry and Physics*, *20*(7), 4047–4058. <https://doi.org/10.5194/acp-20-4047-2020>
- Wolfe, G. M., Nicely, J. M., Clair, St. J. M., Hanisco, T. F., Liao, J., Oman, L. D., et al. (2019). Mapping hydroxyl variability throughout the global remote troposphere via synthesis of airborne and satellite formaldehyde observations. *Proceedings of the National Academy of Sciences of the United States of America*, *116*(23), 11171–11180. <https://doi.org/10.1073/pnas.1821661116>
- Wolter, K., & Timlin, M. S. (2011). El Niño/Southern Oscillation behaviour since 1871 as diagnosed in an extended multivariate ENSO index (MEI.ext). *International Journal of Climatology*, *31*(7), 1074–1087. <https://doi.org/10.1002/joc.2336>
- Zhao, Y., Saunois, M., Bousquet, P., Lin, X., Berchet, A., Hegglin, M. I., et al. (2019). Inter-model comparison of global hydroxyl radical (OH) distributions and their impact on atmospheric methane over the 2000–2016 period. *Atmospheric Chemistry and Physics*, *19*(21), 13701–13723. <https://doi.org/10.5194/acp-19-13701-2019>
- Zhao, Y., Saunois, M., Bousquet, P., Lin, X., Berchet, A., Hegglin, M. I., et al. (2020). Influences of hydroxyl radicals (OH) on top-down estimates of the global and regional methane budgets. *Atmospheric Chemistry and Physics*, *20*(15), 9525–9546. <https://doi.org/10.5194/acp-20-9525-2020>